Dalton Transactions

ROYAL SOCIETY OF CHEMISTRY

PAPER

View Article Online
View Journal | View Issue

Cite this: *Dalton Trans.*, 2025, **54**, 1994

Thermoelectric and electrical properties of triple-conducting multicomponent oxides based on substituted barium cerate-zirconate

M. M. Czudec, *[a] D. Jaworski,[a] J. Budnik,[a] A. Mielewczyk-Gryń,[a] T. Subramani,[b] M. Gazda,[a] A. Navrotsky[b] and T. Miruszewski[a]

Received 10th July 2024,
Accepted 13th November 2024

DOI: 10.1039/d4dt01992j

rsc.li/dalton

Multicomponent oxides often have exceptional thermal stability and interesting electronic properties. The present work presents the thermoelectric and electrical properties of the $Ba(Zr_{0.2}Hf_{0.2}Sn_{0.2}Ti_{0.2}Fe_{0.2})O_{3-\delta}$ and $Ba(Zr_{0.1}Hf_{0.1}Sn_{0.1}Ti_{0.1}Co_{0.1}Ce_{0.1}Bi_{0.1}Fe_{0.1}Y_{0.1}Zn_{0.1})O_{3-\delta}$ multicomponent perovskites. Single-phase cubic perovskites were synthesized using the solid-state reaction method. They were characterized using X-ray diffraction, drop-solution calorimetry, and thermogravimetry methods. The total electrical conductivity and Seebeck coefficient measurements were performed in dry and wet air at temperatures between 600 and 1050 K. It was found that $Ba(Zr_{0.1}Hf_{0.1}Sn_{0.1}Ti_{0.1}Co_{0.1}Ce_{0.1}Bi_{0.1}Fe_{0.1}Y_{0.1}Zn_{0.1})O_{3-\delta}$ is thermodynamically less stable than $Ba(Zr_{0.2}Hf_{0.2}Sn_{0.2}Ti_{0.2}Fe_{0.2})O_{3-\delta}$. Moreover, this oxide incorporates a higher amount of water and exhibits higher conductivity and lower Seebeck coefficient. Charge transport in both perovskites can be assigned to the small-polaron hopping process *via* electron holes. An interesting temperature dependence of the Seebeck coefficient was found and, at temperatures above 750 K, related to hopping between energetically inequivalent states.

1. Introduction

The Seebeck effect is a thermoelectric phenomenon in which the temperature difference applied to a material is converted into electrical voltage. A system of two materials forming two junctions having different temperatures may function as a thermoelectric generator. The thermoelectric voltage, besides being a potential way of electric energy harvesting through utilizing various heat sources, also provides additional information on electronic transport. For instance, in materials conducting predominantly either electrons or electron holes, the sign of the majority charge carrier may be determined. The generated thermoelectric voltage value can be negative, which indicates electron conduction, or positive for materials with a predominant hole conduction. Moreover, the Seebeck coefficient and its temperature dependence can give indirect information on the structural or electronic disorder.[1]

The studies of oxide thermoelectric materials began in 1997 when Terasaki *et al.* reported a high positive Seebeck coefficient of ~100 μV K^{-1} at 300 K in $NaCo_2O_4$.[2] Later, more studies on the thermoelectric properties of oxides, for example ZnO,[3] doped $SrTiO_3$,[4] doped $MgWO_4$,[5] and many other oxides, were published.[6,7] Recently, multicomponent oxides have been investigated in terms of their thermoelectric properties. For example, Gild *et al.* studied oxides based on the $(Hf_{0.25}Zr_{0.25}Ce_{0.25}Y_{0.25})O_{2-\delta}$ fluorite phases. Compared to 8 mol% Y_2O_3-stabilized ZrO_2 (8YSZ), they exhibited lower electrical and thermal conductivities, likely due to enhanced phonon scattering originating from the short-range disorder caused by the presence of multiple cations and lattice strain.[8] Zhang *et al.*[9] studied the synthesis and properties of $(Ca_{0.2}Sr_{0.2}Ba_{0.2}La_{0.2}Pb_{0.2})TiO_3$. These materials exhibited high Seebeck coefficients (272 μV K^{-1} at 1073 K) and low thermal conductivity. Moreover, the Seebeck coefficient was negative between 323 and 1073 K, indicating n-type conduction. The maximum thermoelectric power factor was 0.25 μW (m K^2)$^{-1}$ at 1073 K for samples annealed at 1573 K. Kumar *et al.*[10] examined high-entropy oxide-based wolframites: $(CoCuNiFeZn)_{1-x}Ga_xWO_4$. In $(CoCuNiFeZn)WO_4$, the total thermal conductivity was significantly reduced (~2.1 W m^{-1} K^{-1}) compared to ~11.5 W m^{-1} K^{-1} for $MgWO_4$ due to enhanced phonon scattering. It was also found that the Seebeck coefficient and electrical conductivity depend on the Ga doping. These results show that materials engineering of multicomponent oxides can significantly enhance their thermoelectric properties. Though oxides and multicomponent oxides have interesting thermoelectric properties, they have also one serious drawback

[a]*Institute of Nanotechnology and Materials Engineering, Advanced Materials Centre, Gdańsk University of Technology, Gdańsk, Poland.*
E-mail: martyna.czudec@pg.edu.pl
[b]*Navrotsky Eyring Center for Materials of the Universe, School of Molecular Sciences, Arizona State University, Tempe, AZ 85287, USA*

that hinders their practical applications. Namely, the electrical conductivity of oxides is usually low which significantly limits the thermoelectric power factor P_f ($P_f = \sigma\alpha^2$), where σ is the electrical conductivity and α denotes the Seebeck coefficient. Nevertheless, it is not the only factor that determines the suitability of a material for application in thermoelectric devices. Thermoelectric materials based on metal alloys or intermetallic compounds usually cannot operate above 600 °C due to structural decomposition above this temperature. Though ceramic oxides may exhibit lower electrical conductivity and lower power factors compared to the commercially used metallic alloys *e.g.* Bi_2Te_3, PbTe, SiGe, Bi–Sb system, they have higher chemical and thermal stability. Therefore, oxides are possible to use in waste heat recovery technology, at temperatures even above 1000 °C at which alloys and other commonly studied thermoelectric materials cannot function.

In this work, we report the thermoelectric and electrical properties of $Ba(Zr_{0.2}Hf_{0.2}Sn_{0.2}Ti_{0.2}Fe_{0.2})O_{3-\delta}$ and $Ba(Zr_{0.1}Hf_{0.1}Sn_{0.1}Ti_{0.1}Co_{0.1}Ce_{0.1}Bi_{0.1}Fe_{0.1}Y_{0.1}Zn_{0.1})O_{3-\delta}$ multicomponent perovskites. The temperature dependencies of the Seebeck coefficient and the total electrical conductivity studied in dry and humidified air are compared with those of $BaCe_{0.6}Zr_{0.2}Y_{0.2}O_{3-\delta}$ and $BaCe_{0.6}Zr_{0.2}Y_{0.1}Tb_{0.1}O_{3-\delta}$.

2. Experimental methods

Polycrystalline samples of nominal compositions $Ba(Zr_{0.2}Hf_{0.2}Sn_{0.2}Ti_{0.2}Fe_{0.2})O_{3-\delta}$ and $Ba(Zr_{0.1}Hf_{0.1}Sn_{0.1}Ti_{0.1}Co_{0.1}Ce_{0.1}Bi_{0.1}Fe_{0.1}Y_{0.1}Zn_{0.1})O_{3-\delta}$, as well as $BaCe_{0.6}Zr_{0.2}Y_{0.2}O_{3-\delta}$ and $BaCe_{0.6}Zr_{0.2}Y_{0.1}Tb_{0.1}O_{3-\delta}$ were synthesized using a solid-state reaction method. In the text below, $Ba(Zr_{0.2}Hf_{0.2}Sn_{0.2}Ti_{0.2}Fe_{0.2})O_{3-\delta}$ and $Ba(Zr_{0.1}Hf_{0.1}Sn_{0.1}Ti_{0.1}Co_{0.1}Ce_{0.1}Bi_{0.1}Fe_{0.1}Y_{0.1}Zn_{0.1})O_{3-\delta}$ are denoted as MO5 and MO10, respectively. The following reagents: $BaCO_3$, TiO_2, Fe_2O_3, HfO_2, ZrO_2, SnO_2, Co_3O_4, CeO_2, Bi_2O_3, Y_2O_3, ZnO and Tb_4O_7 with at least 99.9% purity were used. The precursors in stoichiometric proportions were ball-milled for 24 hours. ZrO_2 cups and milling balls were used, while the rotation speed of the mill was set at 600 rpm. The powders were then calcined at 1223 K for 24 h. Subsequently, the powders, with the addition of 1 wt% of PVB were uniaxially pressed (350 MPa) into cuboidal pellets with a size of 10 mm × 2 mm × 1 mm and sintered in air for 10 h at 1473 K in the case of MO10 and at 1673 K for other samples in the case of MO5. The lower sintering temperature applied for MO10 was due to the presence of cobalt in this sample.

The crystal structure and phase composition were studied by X-ray diffraction (XRD) using a Phillips X'Pert Pro diffractometer with a Cu K_α anode. The XRD patterns were analyzed using HighScore Plus XRD Analysis Software. The crystal structure was refined using the Rietveld method. As initial data, the $BaZrO_3$ cubic structure ($Pm\bar{3}m$ space group) with a = 4.181 Å unit cell parameter (COD 1538369) was used.

Thermogravimetric (TG) analysis was carried out on a Netzsch STA 449 DSC to study water uptake. Before the TG analysis, powdered samples were annealed at 1073 K for 5 h in dry gas (p_{H_2O} *ca.* 5.0×10^{-5} atm) to remove water and surface carbon dioxide. Then they were cooled and kept at 573 K for 2 h and, after that, the gas was switched from dry to wet air (p_{H_2O} *ca.* 2.3×10^{-2} atm). The samples were humidified for 2 h and then the gas was switched back to the dry one for another 2 h. The difference between the mass recorded in the dry and wet atmospheres (Δm_{H_2O}) enabled the estimation of the molar protonic defect concentration $[OH_O^\bullet]$.

To study electrical properties, four platinum electrodes were painted on the surface of the pellets and platinum wires (φ = 0.15 mm) were attached to the electrodes. The electrodes were heated at 1203 K for 3 h in air. Temperature dependences of total electrical conductivity measurements were analysed by electrochemical impedance spectroscopy (EIS) using a Gamry Reference 3000 impedance analyzer in dry and humidified air ($p_{H_2O} \approx 10^{-5}$ atm and $p_{H_2O} \approx 2.3 \times 10^{-2}$ atm, respectively). The measurements were performed in the temperature range 573–1088 K with a step of 50 K. At each temperature, thermodynamic stabilization was achieved after approximately 1 h. The obtained impedance spectra were analyzed using ZView™ software with a suitable electrochemical model containing resistors and CPE elements. Different electrochemical models were used for the MO5 and MO10 samples, due to the different concentrations of electron holes and oxygen vacancies in these materials.

The Seebeck coefficient measurements were performed using the Linseis LSR4 apparatus, modified for measurements in dry and wet air. The measurements were carried out at 623–1073 K in the configuration presented in Fig. 1. Two electrodes T_1 and T_4 enforce a temperature gradient in the sample located between them, while the T_2 and T_3 thermocouples measure the temperature difference ΔT and the generated thermoelectric voltage. The total Seebeck coefficient was calculated *versus* platinum using the ratio between the Seebeck voltage and ΔT. A temperature difference between T_1 and T_4 was between 8 and 11 K and was maintained over the entire temperature range.

High-temperature oxide melt solution calorimetry on predried samples was carried out using a Setaram AlexSYS Tian-Calvet twin microcalorimeter.[11] The calorimeter was calibrated

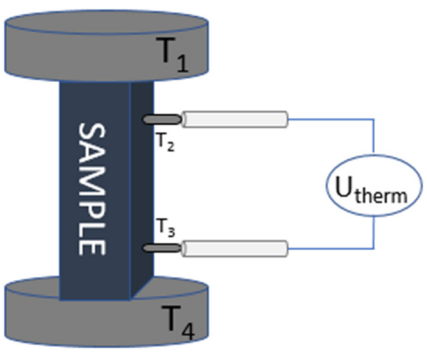

Fig. 1 Experimental scheme of Seebeck coefficient measurement.

Table 1 Thermodynamic cycle used for calculations of formation enthalpies at room temperature

Reaction	ΔH (kJ mol^{-1})
$BaTi_{0.2}Fe_{0.2}Hf_{0.2}Zr_{0.2}Sn_{0.2}O_{3-\delta}$ (s, 298 K) → BaO (dis, 1073 K) + $0.1Fe_2O_3$ (dis, 1073 K) + $0.2ZrO_2$ (dis, 1073 K) + $0.2HfO_2$ (dis, 1073 K) + $0.2SnO_2$ (dis, 1073 K) + $0.2TiO_2$ (dis, 1073 K)	$\Delta H_1 = \Delta H_{ds}$
BaO (s, 298 K) → BaO (dis, 1073 K)	ΔH_2
Fe_2O_3 (s, 298 K) → Ln_2O_3 (dis, 1073 K)	ΔH_3
ZrO_2 (s, 298 K) → ZrO_2 (dis, 1073 K)	ΔH_4
HfO_2 (s, 298 K) → HfO_2 (dis, 1073 K)	ΔH_5
SnO_2 (s, 298 K) → SnO_2 (dis, 1073 K)	ΔH_6
TiO_2 (s, 298 K) → TiO_2 (dis, 1073 K)	ΔH_7
BaO (s, 298 K) + $0.1Fe_2O_3$ (s, 298 K) + $0.2ZrO_2$ (s, 298 K) + $0.2HfO_2$ (s, 298 K) + $0.2SnO_2$ (s, 298 K) + $0.2TiO_2$ (s, 298 K) → $BaTi_{0.2}Fe_{0.2}Hf_{0.2}Zr_{0.2}Sn_{0.2}O_{3-\delta}$ (s, 298 K)	$\Delta H_{f,\,ox}$

$\Delta H_{f,\,ox} = -\Delta H_1 + \Delta H_2 + 0.1\Delta H_3 + 0.2\Delta H_4 + 0.2\Delta H_5 + 0.2\Delta H_6 + 0.2\Delta H_7$

against the heat content of α-Al_2O_3 (99.99%). Pressed sample pellets (~5 mg) were dropped from ambient temperature into the calorimeter containing the solvent, molten sodium molybdate ($3Na_2O{\cdot}4MoO_3$), in a silica glass crucible at 1073 K. All experiments used oxygen bubbling through the solvent at 5 mL min^{-1} to aid dissolution and prevent local saturation of the solvent. The thermodynamic cycle used to calculate the enthalpy of formation is described in Table 1.

3. Results and discussion

Fig. 2 presents diffractograms for the MO5 and MO10 samples. All diffraction maxima correspond to the cubic perovskite structure of the $BaZrO_{3-\delta}$ phase with the *Pm*$\bar{3}$*m* space group. The unit cell parameters calculated by the Rietveld refinement are 4.1120(2) Å for MO5 and 4.1958(1) Å for MO10. The unit cell parameter of $Ba(Zr_{0.2}Hf_{0.2}Sn_{0.2}Ti_{0.2}Fe_{0.2})O_{3-\delta}$ is lower than that of $Ba(Zr_{0.1}Hf_{0.1}Sn_{0.1}Ti_{0.1}Co_{0.1}Ce_{0.1}Bi_{0.1}Fe_{0.1}Y_{0.1}Zn_{0.1})O_{3-\delta}$ which is related to a different average ionic radius of the B-cation (0.655 Å and 0.7075 Å) in both perovskites.

The SEM-EDS analysis results for the MO5 and MO10 samples are presented in Table 2. The table contains the average data obtained on 10 measurement spots. The chemical compositions based on the atomic content of the elements are $Ba_{1.34}Zr_{0.21}Hf_{0.17}Sn_{0.26}Ti_{0.13}Fe_{0.23}O_{2.38}$ for MO5 and $Ba_{1.42}Zr_{0.09}Hf_{0.11}Sn_{0.11}Ti_{0.07}Co_{0.10}Ce_{0.10}Bi_{0.09}Fe_{0.10}Y_{0.12}Zn_{0.11}O_{3.28}$ for MO10. They were estimated assuming that the entire B sublattice of the perovskite constitutes a fixed 1 mole of cations. Since the total maximum error of the sum of B cation

Table 2 Quantitative results of EDS analysis collected from 10 different spots for MO5 and MO10 samples. Measurement uncertainty was determined as the standard deviation from the mean value

	Atomic content (%)	Measurement uncertainty (%)
$Ba(Zr_{0.2}Hf_{0.2}Sn_{0.2}Ti_{0.2}Fe_{0.2})O_{3-\delta}$ (MO5)		
Ba	28.49	0.92
O	50.4	1.4
Zr	4.44	0.23
Sn	5.41	0.36
Ti	2.84	0.39
Fe	4.81	0.68
Hf	3.62	0.37
$Ba(Zr_{0.1}Hf_{0.1}Sn_{0.1}Ti_{0.1}Co_{0.1}Ce_{0.1}Bi_{0.1}Fe_{0.1}Y_{0.1}Zn_{0.1})O_{3-\delta}$ (MO10)		
Ba	25.0	2.8
O	57.5	4.5
Y	2.18	0.55
Zr	1.74	0.51
Bi	1.60	0.32
Sn	1.84	0.63
Ti	1.3	0.6
Ce	1.77	0.71
Fe	1.82	0.45
Co	1.79	0.48
Hf	1.56	0.37
Zn	1.90	0.59

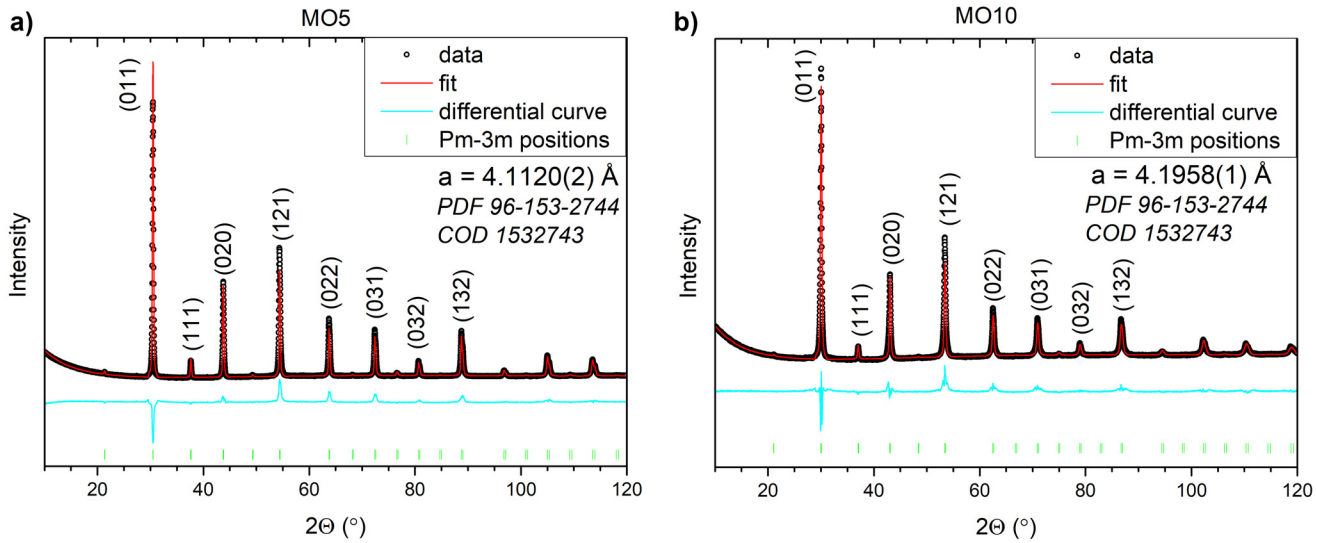

Fig. 2 X-ray diffraction patterns with Rietveld refinement profiles and Miller indices of (a) MO5 and (b) MO10 samples.

amount is quite high, this is the reason for the apparent nonstoichiometry in the Ba and O sites. Moreover, the relatively high measurement uncertainty of EDS (especially when determining oxygen content) should be taken into consideration. Nevertheless, the B-cation compositions are close to that intended during the materials synthesis process. This shows that the cations were well distributed during the solid-state synthesis and that no cations significantly evaporated during the synthesis process.

The results of thermogravimetric analysis after the switch from dry to humid air are shown in Fig. 3. It can be seen that the mass of both oxides increases in humid air. In the case of MO5, the process takes place in one step and the difference in the mass after the switch is much lower than in MO10. The mass of the MO10 sample, after the initial rapid increase, continues to gradually increase at a lower rate. Similar characteristics of the water uptake are observed in $BaCe_{0.6}Zr_{0.2}Y_{0.1}M_{0.1}O_{3-\delta}$ (M = Tb, Pr, Fe)[12] and in double perovskite cobaltite.[13]

The first rapid step of the mass increase could be interpreted as the proton uptake process. In typical proton-conductors, this occurs as a hydration process involving oxygen vacancies.[13]

$$H_2O_{(g)} + V_O^{\bullet\bullet} \leftrightarrow \frac{1}{2}O_{2(g)} + 2OH^{\bullet} \quad (1)$$

On the other hand, in triple-conducting oxides in oxidizing atmospheres, the electron–hole concentration is expected to be quite high. If it is much higher than that of oxygen vacancies, proton defects form through the hydrogenation reaction described by eqn (2).[13,14]

$$H_2O_{(g)} + 2O_O^x + 2h^{\bullet} \leftrightarrow \frac{1}{2}O_{2(g)} + 2OH^{\bullet} \quad (2)$$

$Ba(Zr_{0.2}Hf_{0.2}Sn_{0.2}Ti_{0.2}Fe_{0.2})O_{3-\delta}$ and $Ba(Zr_{0.1}Hf_{0.1}Sn_{0.1}Ti_{0.1}Co_{0.1}Ce_{0.1}Bi_{0.1}Fe_{0.1}Y_{0.1}Zn_{0.1})O_{3-\delta}$ in an oxidizing atmosphere, *e.g.* in air, similarly to other perovskites containing iron, *e.g.* $BaZr_{1-x}Fe_xO_{3-\delta}$,[15] and/or cobalt, *e.g.* $BaCo_xZr_{0.9-x}Sc_{0.1}O_{3-\delta}$,[16] are expected to contain electron–hole charge carriers. Also, cerium, titanium, and bismuth have varying oxidation states contributing to the electronic-type charge carriers. Thus, for the materials studied within this work, the most probable scenario is that the hydrogenation process contributes to proton defect formation which means that the increasing proton concentration leads to a decrease in electron–hole concentration. The nature of the slow increase in the mass observed in $Ba(Zr_{0.1}Hf_{0.1}Sn_{0.1}Ti_{0.1}Co_{0.1}Ce_{0.1}Bi_{0.1}Fe_{0.1}Y_{0.1}Zn_{0.1})O_{3-\delta}$ has not been established so far; however, it was proposed that it may be related to the slow oxidation process.[17–19] A fast proton defect formation competing with slow oxidation, that is filling the oxygen vacancies with oxygen, has also been observed by electrical conductivity relaxation methods. For example, R. Merkle *et al.* described this in Fe-doped $SrTiO_3$.[20]

To determine the electrical conductivity of the compounds, impedance studies were performed. Fig. 4 shows an exemplary Nyquist plot with an electrochemical equivalent circuit used to analyze the data in the software. In Fig. 5, the temperature dependencies of total electrical conductivity in the MO5 and MO10 samples in dry and wet air are presented. Selected electrical properties of the studied materials are collected in Table 3. The electrical conductivity of the MO10 sample is 5–7 times higher than that of MO5. In wet air, the difference in the electrical conductivity levels between the samples is similar to that in dry air. In the studied temperature range and both atmospheres, the electrical conductivity of MO5 and MO10 increases with increasing temperature which signifies that the conduction occurs through the thermally-activated processes. Acceptor-substituted perovskite oxides such as $BaZrO_3$,[16] $BaSnO_3$,[21] $BaHfO_3$,[22] *etc.*, depending on the atmosphere and temperature range, are mixed ionic-electronic conductors, with

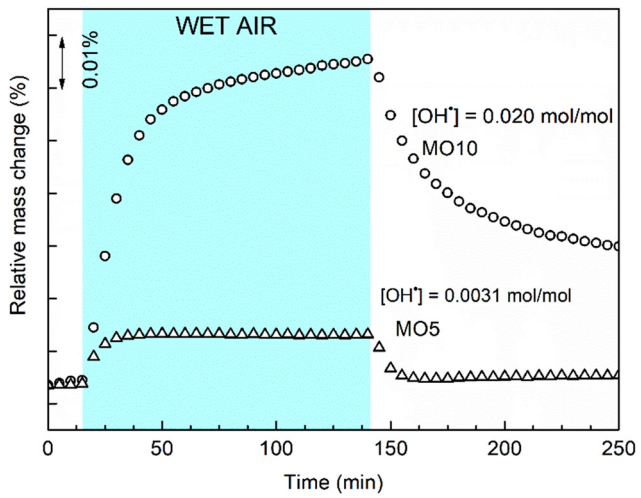

Fig. 3 Mass change of $Ba(Zr_{0.2}Hf_{0.2}Sn_{0.2}Ti_{0.2}Fe_{0.2})O_{3-\delta}$ and $Ba(Zr_{0.1}Hf_{0.1}Sn_{0.1}Ti_{0.1}Co_{0.1}Ce_{0.1}Bi_{0.1}Fe_{0.1}Y_{0.1}Zn_{0.1})O_{3-\delta}$ recorded after isothermal switch at 573 K between dry and humidified air.

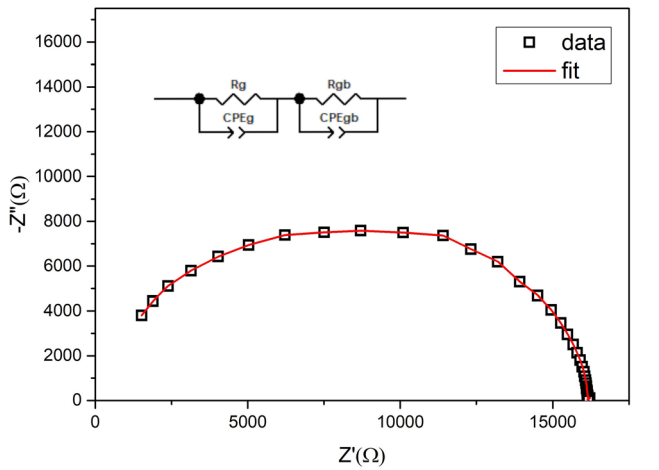

Fig. 4 An exemplary Nyquist plot of the MO5 sample, measured in dry air at 738 K.

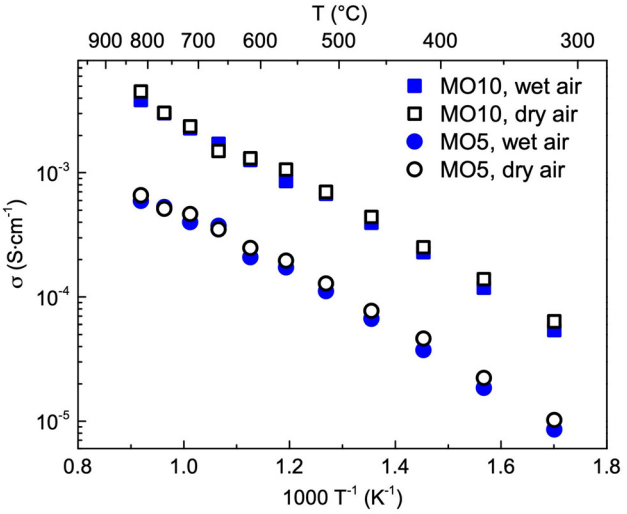

Fig. 5 Temperature dependencies of total electrical conductivity, shown in Arrhenius-type coordinates, for the MO5 and MO10 materials, measured in dry and wet air.

oxygen ions, protons, electrons, and/or electron holes as charge carriers.

In dry atmospheres, the total electrical conductivity can be then expressed by eqn (3) [13]

$$\sigma_{dry} = e[h^{\bullet}]\mu_h + 2e[V_O^{\bullet\bullet}]\mu_{V_O}, \quad (3)$$

where e denotes the elementary electron charge, $[h^{\bullet}]$ and $[V_O^{\bullet\bullet}]$ are electron–hole and oxygen vacancy concentrations, while μ_h and μ_{V_O} are their respective mobilities. In the case of substituted barium zirconate perovskites at temperatures above room temperature, small-polaron hopping is considered the predominant transport mechanism.[23,24] In wet air, protonic conductivity also appears, especially at lower temperatures, where the protonic defect concentration is high. In this case, the total electrical conductivity in wet air contains three terms and can be described as:[13]

$$\sigma_{wet} = e[h^{\bullet}]\mu_h + 2e[V_O^{\bullet\bullet}]\mu_{V_O} + e[OH_O^{\bullet}]\mu_{OH}, \quad (4)$$

where $OH_O^{\bullet}$ denotes a protonic defect and $\mu_{OH^{\bullet}}$ denotes its mobility.

Eqn (5) describes the temperature dependence of electrical conductivity in both ionic[25] and small-polaron hopping transport mechanisms:[26]

$$\sigma = \frac{\sigma_0}{T}\exp\left(-\frac{E_a}{k_B T}\right), \quad (5)$$

where T is the absolute temperature, σ_0/T is a temperature-dependent pre-exponential factor, k_B is the Boltzmann constant and E_a means the activation energy for electrical conduction. The activation energies of total conductivity for MO5 and MO10 in both dry and wet air, determined based on eqn (5), are presented in Table 3. Because of a small change in the slopes of the log $\sigma\left(\frac{1}{T}\right)$ plots around 873 K, the activation energies below and above this temperature are treated separately. Within the measurement uncertainty, the activation energies are similar, regardless of the chemical composition and the atmosphere. In MO5, above 873 K, the activation energy of conduction is slightly lower than that at lower temperatures, whereas in the MO10 oxide, the difference is negligible. Moreover, the activation energy of conduction in dry air observed in MO5 and MO10 is lower than those found for many other similar perovskites. For example, Zając *et al.* reported 1.05 eV for $BaZr_{0.95}Gd_{0.05}O_{2.975}$,[27] Bohn *et al.* for $BaZr_{0.9}Y_{0.1}O_{2.95}$ found 0.9 eV and 1.1 eV,[28] Yang *et al.* in $BaHf_{0.8}Y_{0.2}O_3$ reported E_a equal to be 0.72 eV in dry air[29] while Kim *et al.* found E_a in $BaZr_{1-x}Fe_xO_{3-\delta}$ (x = 0.1, 0.2 and 0.33) respectively to be 0.9, 1.1 and 0.3 eV in dry oxygen.[30] Our previous studies of high-entropy oxides showed activation energies in dry air for $BaZr_{0.2}Sn_{0.2}Ti_{0.2}Hf_{0.2}Ce_{0.2}O_{3-\delta}$, $BaZr_{0.2}Sn_{0.2}Ti_{0.2}Hf_{0.2}Y_{0.2}O_{3-\delta}$, $BaZr_{0.15}Sn_{0.15}Ti_{0.15}Hf_{0.15}Ce_{0.15}Nb_{0.15}Y_{0.1}O_{3-\delta}$ and $BaZr_{1/7}Sn_{1/7}Ti_{1/7}Hf_{1/7}Ce_{1/7}Nb_{1/7}Y_{1/7}O_{3-\delta}$ between 0.98 and 1.55 eV in dry air.[31] We believe that lower activation energy of conduction in $Ba(Zr_{0.2}Hf_{0.2}Sn_{0.2}Ti_{0.2}Fe_{0.2})O_{3-\delta}$ and $Ba(Zr_{0.1}Hf_{0.1}Sn_{0.1}Ti_{0.1}Co_{0.1}Ce_{0.1}Bi_{0.1}Fe_{0.1}Y_{0.1}Zn_{0.1})O_{3-\delta}$ in comparison to barium zirconates substituted with only RE elements is related to the higher content of multi-valent cations *e.g.* Fe, Co, Ce, Ti, and Bi.

Table 3 Values of conductivity, activation energies, E_a, of conduction in dry and wet air, protonic defect concentrations, Seebeck coefficients, and estimated values of the thermoelectric transport activation energy E_S, hopping energy W_H, and polaron formation energy E_p in MO5 and MO10

	$Ba(Zr_{0.2}Hf_{0.2}Sn_{0.2}Ti_{0.2}Fe_{0.2})O_{3-\delta}$		$Ba(Zr_{0.1}Hf_{0.1}Sn_{0.1}Ti_{0.1}Co_{0.1}Ce_{0.1}Bi_{0.1}Fe_{0.1}Y_{0.1}Zn_{0.1})O_{3-\delta}$	
	Wet air	Dry air	Wet air	Dry air
σ (873 K), S cm^{-1}	2.1×10^{-4}	2.5×10^{-4}	1.26×10^{-3}	1.31×10^{-3}
σ (1083 K), S cm^{-1}	5.9×10^{-4}	6.6×10^{-4}	3.85×10^{-3}	4.5×10^{-3}
E_a below 873 K, eV	0.57(2)	0.55(2)	0.54(2)	0.52(4)
E_a above 873 K, eV	0.49(2)	0.48(2)	0.52(2)	0.51(4)
$[OH_O^{\bullet}]$ at 573 K, mol/mol	0.003	—	0.02	—
E_S below 873 K, eV	0.094(15)	0.015(8)	0.019(5)	0.015(5)
W_H below 873 K, eV	0.48(4)	0.54(3)	0.52(3)	0.51(5)
E_p below 873 K, eV	0.96(8)	1.08(6)	1.04(6)	1.0(1)
α (~873 K), μV K^{-1}	420	360	100	100

Similar values of activation energies observed for both materials in dry and wet air suggest two conclusions. The first is that the differences in the numbers and types of elements in $Ba(Zr_{0.2}Hf_{0.2}Sn_{0.2}Ti_{0.2}Fe_{0.2})O_{3-\delta}$ and $Ba(Zr_{0.1}Hf_{0.1}Sn_{0.1}Ti_{0.1}Co_{0.1}Ce_{0.1}Bi_{0.1}Fe_{0.1}Y_{0.1}Zn_{0.1})O_{3-\delta}$ do not significantly affect the potential barrier heights for charge carrier hopping, while the second is a weak influence of the humid atmosphere on the total conductivity. The difference in electrical conductivity between the MO5 and MO10 samples probably originates from the difference in their chemical compositions. The MO10 contains about twice higher acceptor constituent content than MO5, which results in a higher charge carrier concentration.

In the MO5 and MO10 oxides in humid atmospheres protonic defects form (Table 3), but the effect of water uptake on electric transport is not strong. In both samples, the electrical conductivity in dry air is higher than that in humid air. The proton defect formation decreases the concentration of electron holes, and the mobility of the holes is higher than that of protonic defects.[32] This may explain the lower observed level of electrical conductivity in wet air than in dry air in both materials. The difference between the conductivities in dry and humid air is small and decreases with increasing temperature reflecting a decreasing concentration of protonic defects.

Temperature dependences of the Seebeck coefficient are presented in Fig. 6. For comparison, Fig. 6c shows the temperature dependence of the Seebeck coefficient in dry air also for $BaCe_{0.6}Zr_{0.2}Y_{0.2}O_{3-\delta}$ (BCZY) and $BaCe_{0.6}Zr_{0.2}Y_{0.1}Tb_{0.1}O_{3-\delta}$ (BCZYTb).[33,34] BCZY and BCZYTb are materials that exhibit a high protonic conductivity; however, in oxidizing atmospheres such as dry air, the contribution of electron hole conductivity is also high.[17,34] All four oxides show positive Seebeck coefficient values, which confirms that the charge carriers taking part in the transport are electron holes and oxygen vacancies.[35–38] MO5 exhibits a much higher value of the Seebeck coefficient, about ~360 μV K^{-1} at 350 °C, whereas, for the MO10 sample, this value is over three times lower (~115 μV K^{-1}).

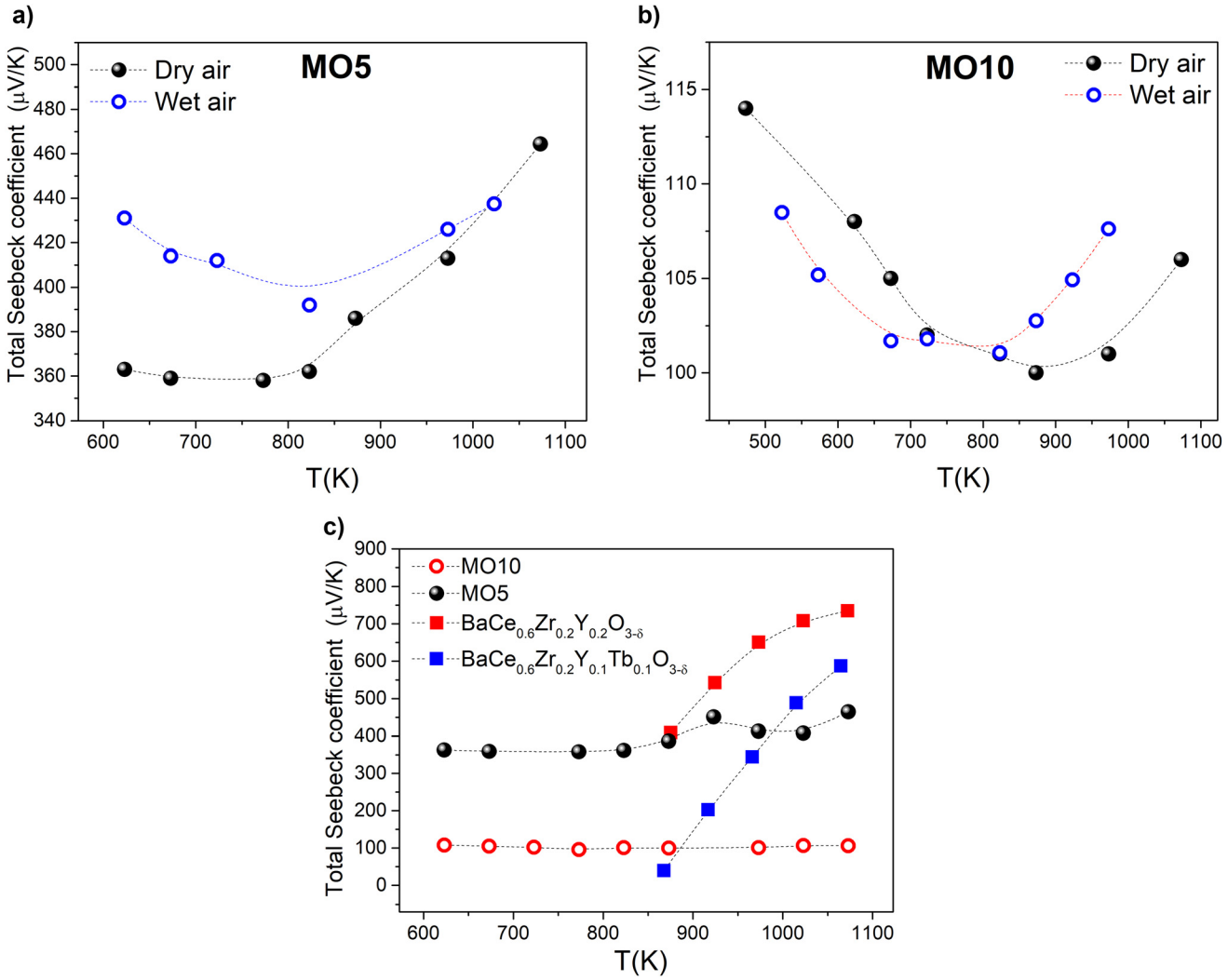

Fig. 6 Comparison of the temperature dependencies of the Seebeck coefficient for (a) MO5 and (b) MO10 samples measured in dry air as well as well-known protonic conductors – (c) BCZY and BCZY doped with terbium.

Such a difference persists throughout the entire studied temperature range. It may be explained by a typical decrease of the Seebeck coefficient with increasing charge carrier concentration. As proposed above, a higher conductivity in MO10 is related to a higher content of multi-valent cations in comparison to MO5. Assuming that the ratio of the conductivities of both oxides, $\sigma_{MO10}/\sigma_{MO5}$, which is between approximately 5 and 7, originates mainly from higher electron hole concentration in MO10, it might explain the difference between the Seebeck coefficients ($\alpha_{MO5}/\alpha_{MO10}$ is about 4). However, we believe that this requires more studies.

The values of the Seebeck coefficient obtained for the MO5 and MO10 samples were compared with the values for various oxides with a perovskite structure. For example, Mubashir *et al.* obtained a value of about 200 μV K^{-1} at 600 K in undoped $BaZrO_3$,[39] Al Azar *et al.* achieved a slightly higher value for such a compound by substituting Hf instead of Zr and reached approximately 250 μV K^{-1} at the same temperature.[40] Jalan *et al.* reported a large Seebeck coefficient in thin $SrTiO_3$ films as high as ~500 μV K^{-1}, however at room temperature.[41]

Both $Ba(Zr_{0.2}Hf_{0.2}Sn_{0.2}Ti_{0.2}Fe_{0.2})O_{3-\delta}$ and $Ba(Zr_{0.1}Hf_{0.1}Sn_{0.1}Ti_{0.1}Co_{0.1}Ce_{0.1}Bi_{0.1}Fe_{0.1}Y_{0.1}Zn_{0.1})O_{3-\delta}$ oxides show qualitatively similar temperature dependences of the Seebeck coefficients. Below approximately 823 K, the Seebeck coefficient decreases with increasing temperature, and then, after reaching a minimum, it begins to increase with increasing temperature. An increase of α with temperature is also observed in $BaCe_{0.6}Zr_{0.2}Y_{0.2}O_{3-\delta}$ and $BaCe_{0.6}Zr_{0.2}Y_{0.1}Tb_{0.1}O_{3-\delta}$. On the other hand, in $BaZrO_3$ and $Ba(Zr, Y)O_3$ which do not contain multi-valent cations, the Seebeck coefficient decreases with increasing temperature.[42] In hopping conduction, the expression describing the temperature dependence of the Seebeck coefficient is the sum of two terms (eqn (6)).

$$\alpha = (T\Delta S + E_T)/qT \quad (6)$$

The first term includes the average change of the entropy (ΔS) of the material when a charge carrier is injected into it, while the second one is proportional to the average vibrational energy E_T transported by a hopping charge carrier of the charge q.[43] In many oxides with a polaron hopping conduction, a decrease of α with temperature is observed,[44,45] so only the first term is considered as significantly influencing temperature dependence of the Seebeck coefficient. For these materials, α may be described by the Mott formula (eqn (7)):[36]

$$\alpha = \frac{k}{|e|}\left(\frac{E_S}{kT} + \beta'\right), \quad (7)$$

where e denotes an elemental charge of an electron; E_S is a thermoelectric transport activation energy (the generation energy of the charge carriers) and β' is a constant of proportionality between the heat transfer and the kinetic energy of the charge carriers. On the other hand, in materials in which the hopping conduction occurs between energetically non-equivalent states, the second term in eqn (7) becomes important. If the distribution of these states is relatively broad, which may be expected in materials composed of different cations occupying the same lattice sites, averaging of this term leads to a contribution to the Seebeck coefficient which increases linearly with temperature: $(k/q)(8CkT)$, where the C constant depends on the number of nearest neighbours, the intersite transfer energy, and the small-polaron binding energy.[24] For instance, the Seebeck coefficient increasing with temperature was observed in $Y_{1-x}M_xCrO_3$ (M = Mg, Ca, Sr, and Ba) perovskites,[46] boron carbide,[43] and many organic materials.[47] Summing up, we propose that below 823 K the Seebeck coefficient of MO5 and MO10 decreases with increasing temperature following eqn (7), while above that temperature the polaron hopping between energetically disordered states causes α to increase with temperature. It is currently difficult to explain why the disorder being higher concerning kT at lower temperatures affects the thermoelectric properties more strongly at higher temperatures, though at a temperature at which the minimum of the Seebeck coefficient is observed, also a subtle change in the activation energy of conduction occurs. A hypothesis that could explain this is that at lower temperatures not all sites are available for polaron hopping. The results of DFT calculations performed for $BaZrO_3$,[48] $BaCeO_3$,[49] $BaTiO_3$,[50] and $BaSnO_3$ [51] perovskites show that the hole-polaron self-trapping energy (between 0.05 and 0.20 eV) is much lower than the energy of hole polaron trapping by acceptor dopants (between 0.3 and 0.8 eV). Values of trapping energies and the extent of polaron localization depend on the chemical nature of an acceptor and its concentration,[48] which makes the situation in the multicomponent perovskites even more complex with possibly a wide distribution of polaron trapping energies. As a result, in the lower temperature range, polarons trapped in deep traps may be immobile, simultaneously excluding these states from the charge transport. Nevertheless, to validate that, calculations should be performed.

At lower temperatures, eqn (7) allows the determination of the thermoelectric transport activation energy (E_S). The values based on the temperature dependence of α are between 15 and 90 meV (Table 3). Such low values were also observed in other oxides; for example, Jibri *et al.* found thermoelectric transport in $LaCrO_3$ with activation energy as low as 2–5 meV.[52] The values of E_S are much lower than the activation energies for conduction, agreeing with the small-polaron transport mechanism.[14,53]

The activation energy for hopping conduction (E_a) is a sum of the energy required for generating a charge carrier – E_S, the energy required for polaron hopping toward an adjacent site – W_H, and the electron transfer integral – J. It is presented by eqn (8):

$$E_a = E_S + W_H - J \quad (8)$$

Neglecting the electron transfer integral J (usually much lower than E_a and E_S) enables the extraction of energy required for polaron hopping W_H:

$$W_H = E_a - E_S \quad (9)$$

This equation also enables the calculation of the polaronic defects formation energy as:

$$E_p = 2W_H \quad (10)$$

where E_p stands for polaron binding energy.[26]

It can be seen that the polaron hopping energy and the energy of polaron formation (Table 3) found for both oxides, in particular in dry conditions, are similar. The physical meaning of E_p is the difference between electron hole polaron band localized states and the conduction band, which in the studied materials is mostly related to the B-cation 4d and 4f states.[36,37]

In a wet atmosphere, temperature dependences of the Seebeck coefficients of both oxides are similar to those in dry air; however, an interesting difference between the characteristics of MO5 and MO10 may be seen. The MO5 sample behaves as expected for a mixed electron hole and proton conductor: the values of α in wet air are higher than those in dry air, with the difference becoming smaller with increasing temperature. A higher Seebeck coefficient in wet air is related to a lower concentration of electron holes since the proton defect formation by the hydrogenation process occurs at the expense of electron holes (eqn (2)). At high temperatures the concentration of proton defects is very low, so the Seebeck coefficient becomes equal to that in dry air. In contrast to MO5, the Seebeck coefficient of the MO10 sample in wet air changes in an unexpected way. In particular, lower values of α in wet air compared to those in dry air below 773 K and higher above this temperature are intriguing. Knowing that the water uptake of MO10 is almost an order of magnitude higher than that of MO5, one would expect a large decrease in the electron hole concentration resulting in higher α. Since we observe both lower α and lower hole concentration, this suggests that the proton defects in this material influence not only the electron hole concentration but also the material properties as a medium in which thermoelectric transport occurs. It should be also noted that the water uptake of MO10 proceeds with a different kinetics than in MO5, that is with a continuous mass increase occurring after the first abrupt step.

Fig. 7 presents the temperature dependencies of power factor (PF) for samples MO5 and MO10. As can be seen, no significant differences were observed between measurements taken in dry and wet air.

A notable difference between PF values was observed between the analysed materials. For example, at 1038 K the MO5 sample has a value of ~10 nW m^{-1} K^{-2} while at the same temperature, a sample with 10 components in the B-sublattice has a value of 3.3 nW m^{-1} K^{-2}. Specifically, the power factor of MO5 is over three times higher than that in MO10. This can be attributed to the about four times higher Seebeck coefficient of the MO5 sample in comparison to the MO10. It is visible that both samples demonstrate relatively low PF values. Many oxides present much higher values of PF than those obtained in this work. For example, Van Nong *et al.* presented materials from the group of $Ca_{2.91}R_{0.09}Co_2O_6$ (R = Gd, Tb, Dy, and Ho) with PF values 1.95×10^{-5} and 2.9×10^{-5} W m^{-1} K^{-2} at 1100 K

Table 4 Enthalpies of drop solution (ΔH_{ds}) in sodium molybdate solvent at 1073 K used for calculations

Oxide	ΔH_{ds} (kJ mol^{-1})
BaO	−176.48 ± 3.48 (ref. 56)
ZrO_2	29.20 ± 1.2 (ref. 57)
TiO_2	73.74 ± 0.48 (ref. 58)
SnO_2	52.85 ± 0.21 (ref. 59)
HfO_2	23.90 ± 1.1
In_2O_3	12.23 ± 1.03 (ref. 59)
ZnO	20.68 ± 0.7 (ref. 60)
Y_2O_3	−116.34 ± 1.21 (ref. 61)
Fe_2O_3	115.92 ± 1.57 (ref. 62)
Bi_2O_3	8.01 ± 0.53 (ref. 59)
CeO_2	76.78 ± 0.75 (ref. 63–65)[a]

[a] Recalculated from 973 K including the heat content difference.

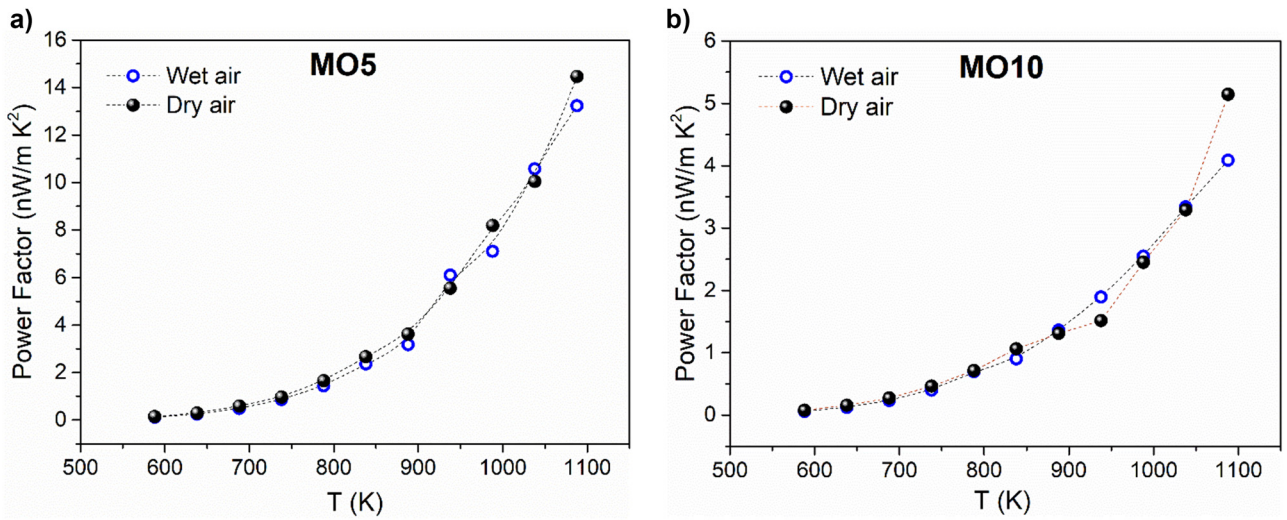

Fig. 7 The power factor values for (a) MO5 and (b) MO10 samples, calculated for dry and wet air.

Table 5 Enthalpies of drop solution (ΔH_{ds}) in sodium molybdate solvent at 1073 K used for calculations and enthalpies of formation from oxides ($\Delta H_{f,\ ox}$) at room temperature for studied materials

Sample	ΔH_{ds} (kJ mol^{-1})	$\Delta H_{f,\ ox}$ (kJ mol^{-1})
$Ba(Zr_{0.2}Hf_{0.2}Sn_{0.2}Ti_{0.2}Fe_{0.2})O_{3-\delta}$ (MO5)	−14.73 ± 0.25	−114.22 ± 6.16
$Ba(Zr_{0.1}Hf_{0.1}Sn_{0.1}Ti_{0.1}Co_{0.1}Ce_{0.1}Bi_{0.1}Fe_{0.1}Y_{0.1}Zn_{0.1})O_{3-\delta}$ (MO10)	−68.7 ± 0.54	−71.68 ± 6.23

for the undoped and Ho-doped samples, respectively.[54] The values of power factor in oxides can be even higher, as 18.9 × 10^{-4} W m^{-1} K^{-2} at ~1100 K for 10% Ag-doped $NaCoO_2$.[55]

To study the energetic stability drop solution calorimetry was applied. Table 4 presents the measured drop solution enthalpy values.

Table 5 presents the drop solution and formation enthalpies from binary oxides of the studied materials. Following our previous studies,[65] the currently studied composition shows the same trend with a lowering of thermodynamic stability with the increasing chemical complexity of the compound.

Moreover, the value obtained for the 5-cation MO5 sample overlaps the previously obtained values for other 5-cation compositions, which range from −102.06 ± 6.27 to −114.25 ± 6.31 kJ mol^{-1}. For the sample with 10 cations the values of enthalpy of formation from oxide (−68.7 ± 0.54 kJ mol^{-1}) are more exothermic than that for previously studied $BaZr_{0.1}Hf_{0.1}Sn_{0.1}Ti_{0.1}Ce_{0.1}Y_{0.1}Sm_{0.1}In_{0.1}Zn_{0.1}Yb_{0.1}O_2$ (−58.66 ± 6.49 kJ mol^{-1}), reflecting slightly higher stability of the currently studied material. This shows that in the case of complex oxides, it is the chemical composition that determines the thermodynamic stability rather than the number of elements by itself. In the current study, the relative basicity of constituent oxides is different from that for previously reported compositions. The governing principles of the role of high chemical complexity on the thermodynamics of oxides have to be established by further studies.

4. Conclusions

Electrical and thermoelectric transport properties of single-phase, polycrystalline multicomponent oxides $Ba(Zr_{0.2}Hf_{0.2}Sn_{0.2}Ti_{0.2}Fe_{0.2})O_{3-\delta}$ (MO5) and $Ba(Zr_{0.1}Hf_{0.1}Sn_{0.1}Ti_{0.1}Co_{0.1}Ce_{0.1}Bi_{0.1}Fe_{0.1}Y_{0.1}Zn_{0.1})O_{3-\delta}$ (MO10) cubic perovskites were studied.

MO5 is thermodynamically more stable than the MO10 oxide, with the enthalpies of formation from oxides of −114.22 ± 6.16 and −71.68 ± 6.23 kJ mol^{-1}, respectively. In humid air, proton defects form in both oxides. The proposed water uptake reaction in MO5 and MO10 materials is hydrogenation with the consumption of electron holes. MO10 incorporated more water than MO5. Moreover, the water uptake of MO10 proceeded in a different way than in MO5, that is with a continuous mass increase occurring after the first abrupt step.

Electrical conductivity in MOs shows a thermally activated mechanism in the atmosphere of dry and wet air, characteristic of compounds based on Ba(Ce, Zr)O_3. A dominant mechanism of conduction in these materials is the transport of small hole polarons. The conductivity of $Ba(Zr_{0.1}Hf_{0.1}Sn_{0.1}Ti_{0.1}Co_{0.1}Ce_{0.1}Bi_{0.1}Fe_{0.1}Y_{0.1}Zn_{0.1})O_{3-\delta}$ was 5–7 times higher than that of $Ba(Zr_{0.2}Hf_{0.2}Sn_{0.2}Ti_{0.2}Fe_{0.2})O_{3-\delta}$ which can be explained by a higher concentration of electron holes. A small effect of p_{H_2O} on charge transport is observed in both studied oxides.

The Seebeck coefficient is positive in both ceramics, confirming electron–hole transport. A higher charge carrier concentration in the MO10 sample results in a much lower Seebeck coefficient than MO5. The temperature dependence of the Seebeck coefficient is discussed. It was interpreted as related to the small polaron hopping between energetically inequivalent states.

Data availability

The data supporting this article have been included in the manuscript.

Conflicts of interest

There is no conflict to declare.

Acknowledgements

The research was financially supported by the National Science Centre (NCN), Poland within the project 2019/35/B/ST5/00888. The calorimetric studies were supported by the U.S. Department of Energy, grant DE-03ER46053.

References

1 M. Wang, C. Bi, L. Li, S. Long, Q. Liu, H. Lv, N. Lu, P. Sun and M. Liu, Thermoelectric Seebeck effect in oxide-based resistive switching memory, *Nat. Commun.*, 2014, **5**(1), 4598.
2 I. Terasaki, Y. Sasago and K. Uchinokura, Large Thermoelectric Power in $NaCo_2O_4$ Single Crystals, *Phys. Rev. B: Condens. Matter Mater. Phys.*, 1997, **56**, R12685–R12687.
3 K. P. Ong, D. J. Singh and P. Wu, Analysis of the thermoelectric properties of n-type ZnO, *Phys. Rev. B: Condens. Matter Mater. Phys.*, 2011, **83**(11), 115110.

4 H. Muta, K. Kurosaki and S. Yamanaka, Thermoelectric properties of rare earth doped $SrTiO_3$, *J. Alloys Compd.*, 2003, **350**(1–2), 292–295.
5 J. Wang, *et al.*, Energetic properties of new nanothermites based on in situ $MgWO_4$-rGO, $CoWO_4$-rGO and Bi_2WO_6-rGO, *Chem. Eng. J.*, 2022, **431**, 133491.
6 S. A. Khandy and D. C. Gupta, Electronic structure, magnetism and thermoelectric properties of double perovskite Sr_2HoNbO_6, *J. Magn. Magn. Mater.*, 2018, **458**, 176–182.
7 L. Yang, *et al.*, High performance thermoelectric materials: progress and their applications, *Adv. Energy Mater.*, 2018, **8**(6), 1701797.
8 J. Gild, M. Samiee, J. L. Braun, T. Harrington, H. Vega, P. E. Hopkins, K. Vecchio and J. Luo, High-entropy fluorite oxides, *J. Eur. Ceram. Soc.*, 2018, **38**, 3578–3584.
9 P. Zhang, Z. Lou, M. Qin, J. Xu, J. Zhu, Z. Shi, Q. Chen, M. J. Reece, H. Yan and F. Gao, High-entropy $(Ca_{0.2}Sr_{0.2}Ba_{0.2}La_{0.2}Pb_{0.2})TiO_3$ perovskite ceramics with A-site short-range disorder for thermoelectric applications, *J. Mater. Sci. Technol.*, 2022, **97**, 182–189.
10 A. Kumar, A. Moll, M. N. Mouhamadsiradjoudine, F. Brisset, D. Berardan and N. Dragoe, Thermoelectric Properties of High–Entropy Wolframite Oxide:(CoCuNiFeZn) 1− xGa_xWO_4, *Phys. Status Solidi RRL*, 2024, **18**(3), 2300372.
11 A. Navrotsky, Progress and new directions in calorimetry: A 2014 perspective, *J. Am. Ceram. Soc.*, 2014, **97**(11), 3349–3359.
12 S. L. Wachowski, I. Szpunar, M. H. Sørby, A. Mielewczyk-Gryń, M. Balaguer, C. Ghica, M. C. Istrate, M. Gazda, A. E. Gunnæs, J. M. Serra, T. Norby and R. Strandbakke, Structure and water uptake in $BaLnCo_2O_{6-\delta}$ (Ln = La, Pr, Nd, Sm, Gd, Tb and Dy), *Acta Mater.*, 2020, **199**, 297–310.
13 T. Norby, Proton conductivity in perovskite oxides, in *Perovskite oxide for solid oxide fuel cells*, Springer US, Boston, MA, 2009, pp. 217–241.
14 R. Merkle, *et al.*, Oxides with mixed protonic and electronic conductivity, *Annu. Rev. Mater. Res.*, 2021, **51**, 461–493.
15 D. Kim, S. Miyoshi, T. Tsuchiya and S. Yamaguchi, Percolation conductivity in BaZrO3–BaFeO3 solid solutions, *Solid State Ionics*, 2014, **262**, 875–878.
16 H. Uehara, A. Ishii, I. Oikawa and H. Takamura, Preparation and mixed proton-hole conductivity of barium zirconate doped with scandium and cobalt, *Int. J. Hydrogen Energy*, 2022, **47**(8), 5577–5584.
17 J. Budnik, A. Mielewczyk-Gryń, M. Gazda and T. Miruszewski, Water uptake kinetics and electrical transport in $BaCe_{0.6}Zr_{0.2}Y_{0.1}M_{0.1}O_{3-\delta}$ (M = Tb, Pr, Fe) protonic conductors, *J. Mater. Chem. A*, 2023, **11**(25), 13389–13398.
18 J. Budnik, A. Mielewczyk-Gryń, M. Gazda and T. Miruszewski, Influence of iron content on water uptake and charge transport in $BaCe_{0.6}Zr_{0.2}Y_{0.2-x}Fe_xO_{3-\delta}$ triple-conducting oxides, *J. Mater. Chem. A*, 2024, **12**(24), 14569–14582.
19 W. Skubida, D. Jaworski, A. Mielewczyk-Gryń, S. Wachowski, T. Miruszewski, K. Cichy, ..., and M. Gazda, Hydration, Structural and Electrical Properties of $BaZr_{1/8}Hf_{1/8}Sn_{1/8}Ti_{1/8}Y_{1/8}In_{1/8}Sm_{1/8}Yb_{1/8}O_{3-x}$ High-Entropy Oxide, available at SSRN 4147298.
20 R. Merkle, W. Sitte and J. Maier, Water incorporation into materials with three mobile carriers: Two-fold relaxation of the electromotive force in Fe-doped SrTiO3 and importance of hole trapping, *Solid State Ionics*, 2020, **347**, 115174.
21 G. N. Starostin, M. T. Akopian, G. K. Vdovin, I. A. Starostina, G. Yang and D. A. Medvedev, Transport properties of highly dense proton-conducting $BaSn_{1-x}In_xO_{3-\delta}$ ceramics, *Int. J. Hydrogen Energy*, 2024, **69**, 306–316.
22 W. Yang, C. Han, Y. Li, H. Zhou, S. Liu, L. Wang, Z. He and L. Dai, Influence of rare-earth doping on the phase composition, sinterability, chemical stability and conductivity of $BaHf_{0.8}Ln_{0.2}O_{3-\delta}$ (Ln = Yb, Y, Dy, Gd) proton conductors, *Int. J. Hydrogen Energy*, 2021, **46**(72), 35678–35691.
23 M. Swift, A. Janotti and C. G. Van De Walle, Small polarons and point defects in barium cerate, *Phys. Rev. B: Condens. Matter Mater. Phys.*, 2015, **92**, 214114.
24 A. Bendahhou, *et al.*, Impact of rare earth (RE 3+= La 3+, Sm 3+) substitution in the A site perovskite on the structural, and electrical properties of Ba $(Zr_{0.9}Ti_{0.})O_3$ ceramics, *RSC Adv.*, 2022, **12**(18), 10895–10910.
25 J. A. Kilner and R. J. Brook, A study of oxygen ion conductivity in doped non-stoichiometric oxides, *Solid State Ionics*, 1982, **6**(3), 237–252.
26 I. G. Austin and N. F. Mott, Polarons in crystalline and non-crystalline materials, *Adv. Phys.*, 1969, **18**(71), 41–102.
27 W. Zając, D. Rusinek, K. Zheng and J. Molenda, Applicability of Gd-Doped $BaZrO_3$, $SrZrO_3$, $BaCeO_3$ and $SrCeO_3$ Proton Conducting Perovskites as Electrolytes for Solid Oxide Fuel Cells, *Cent. Eur. J. Chem.*, 2013, **11**, 471–484.
28 H. G. Bohn and T. Schober, Electrical Conductivity of the High-Temperature Proton Conductor BaZr0.9Y0.1O2.95, *J. Am. Ceram. Soc.*, 2000, **83**, 768–772.
29 W. Yang, L. Wang, Y. Li, H. Zhou, Z. He, C. Han and L. Dai, An easily sintered, chemically stable indium and tin co-doped barium hafnate electrolyte for hydrogen separation, *J. Alloys Compd.*, 2021, **868**, 159117.
30 D. Y. Kim, S. Miyoshi, T. Tsuchiya and S. Yamaguchi, Defect chemistry and electrochemical properties of $BaZrO_3$ heavily doped with Fe, *ECS Trans.*, 2012, **45**(1), 161.
31 M. Gazda, T. Miruszewski, D. Jaworski, A. Mielewczyk-Gryń, W. Skubida, S. Wachowski, P. Winiarz, K. Dzierzgowski, M. Łapiński, I. Szpunar and E. Dzik, Novel class of proton conducting materials—high entropy oxides, *ACS Mater. Lett.*, 2020, **2**(10), 1315–1321.
32 M. Huse, T. Norby and R. Haugsrud, Effects of A and B site acceptor doping on hydration and proton mobility of LaNbO4, *Int. J. Hydrogen Energy*, 2012, **37**(9), 8004–8016.
33 T. Miruszewski, K. Dzierzgowski, P. Winiarz, S. Wachowski, A. Mielewczyk-Gryń and M. Gazda, Structural Properties and Water Uptake of SrTi1− xFexO3− x/2− δ, *Materials*, 2020, **13**(4), 965.
34 D. Kim, D. Lee and J. H. Joo, Effect of Y-doping on the phase relation and electrical properties of Fe-doped $BaZrO_3$, *J. Eur. Ceram. Soc.*, 2018, **38**, 535–542.

35 B. Xu and M. J. Verstraete, First principles explanation of the positive Seebeck coefficient of lithium, *Phys. Rev. Lett.*, 2014, **112**(19), 196603.
36 Y. Natanzon, A. Azulay and Y. Amouyal, Evaluation of polaron transport in solids from first–principles, *Isr. J. Chem.*, 2020, **60**(8–9), 768–786.
37 M. Aycibin, B. Erdinc and H. Akkus, Electronic Structure and Lattice Dynamics of $BaCeO_3$ Compound in Cubic Phase, *J. Electron. Mater.*, 2014, **43**, 4301–4307.
38 R. Terki, *et al.*, Full potential calculation of structural, elastic and electronic properties of $BaZrO_3$ and $SrZrO_3$, *Phys. Status Solidi B*, 2005, **242**(5), 1054–1062.
39 S. Mubashir, M. K. Butt, M. Yaseen, J. Iqbal, M. Iqbal, A. Murtaza and A. Laref, Pressure induced electronic, optical and thermoelectric properties of cubic $BaZrO_3$: a first principle calculations, *Optik*, 2021, **239**, 166694.
40 S. Al Azar, I. Al-Zoubi, A. A. Mousa, R. S. Masharfe and E. K. Jaradat, Investigation of electronic, optical and thermoelectric properties of perovskite $BaTMO_3$ (TM = Zr, Hf): First principles calculations, *J. Alloys Compd.*, 2021, **887**, 161361.
41 B. Jalan and S. Stemmer, Large Seebeck coefficients and thermoelectric power factor of La-doped $SrTiO_3$ thin films, *Appl. Phys. Lett.*, 2010, **97**(4), 42106.
42 D. Tsvetkov, *et al.*, Thermoelectric behavior of $BaZr_{0.9}Y_{0.1}O_{3-d}$ proton conducting electrolyte, *Membranes*, 2019, **9**(9), 120.
43 C. Wood and D. Emin, Conduction mechanism in boron carbide, *Phys. Rev. B: Condens. Matter Mater. Phys.*, 1984, **29**(8), 4582.
44 J. I. Jung, S. T. Misture and D. D. Edwards, Seebeck coefficient and electrical conductivity of BSCF ($Ba_{0.5}Sr_{0.5}Co_xFe_{1-x}O_{3-\delta}$, $0 \leq x \leq 0.8$) as a function of temperature and partial oxygen pressure, *Solid State Ionics*, 2012, **206**, 50–56.
45 Y. Zheng, M. Zou, W. Zhang, D. Yi, J. Lan, C. W. Nan and Y. H. Lin, Electrical and thermal transport behaviours of high-entropy perovskite thermoelectric oxides, *J. Adv. Ceram.*, 2021, **10**, 377–384.
46 W. J. Weber, C. W. Griffin and J. L. Bates, Electrical and thermal transport properties of the $Y_{1-x}M_xCrO_3$ system, *J. Mater. Res.*, 1986, **1**(5), 675–684.
47 N. Lu, L. Li and M. Liu, A review of carrier thermoelectric-transport theory in organic semiconductors, *Phys. Chem. Chem. Phys.*, 2016, **18**(29), 19503–19525.
48 A. Marthinsen and G. Wahnstrom, Percolation transition in hole-conducting acceptor-doped barium zirconate, *Chem. Mater.*, 2020, **32**(13), 5558–5568.
49 A. J. Rowberg, M. Li, T. Ogitsu and J. B. Varley, Polarons and electrical leakage in $BaZrO_3$ and $BaCeO_3$, *Phys. Rev. Mater.*, 2023, **7**(1), 015402.
50 P. Erhart, A. Klein, D. Åberg and B. Sadigh, Efficacy of the DFT+ U formalism for modeling hole polarons in perovskite oxides, *Phys. Rev. B: Condens. Matter Mater. Phys.*, 2014, **90**(3), 035204.
51 G. Geneste, B. Amadon, M. Torrent and G. Dezanneau, DFT+ U study of self-trapping, trapping, and mobility of oxygen-type hole polarons in barium stannate, *Phys. Rev. B*, 2017, **96**(13), 134123.
52 K. M. Jibri, J. Archana, M. Navaneethan and S. Harish, Small polaron hopping conduction mechanism and enhanced thermoelectric power factor in the perovskite $LaCoO_3$ ceramic, *Phys. Chem. Chem. Phys.*, 2023, **25**(18), 12914–12922.
53 K. Teske, *et al.*, Temperature dependence of electrical conductivity of oxides with a range of stoichiometry under isostoichiometric conditions, *Solid State Ionics*, 2000, **133**(1–2), 121–128.
54 N. Van Nong and M. Ohtaki, Power factors of late rare earth-doped Ca3Co2O6 oxides, *Solid State Commun.*, 2006, **139**(5), 232–234.
55 M. Ito and D. Furumoto, Microstructure and thermoelectric properties of NaxCo2O4/Ag composite synthesized by the poly-merized complex method, *J. Alloys Compd.*, 2008, **450**, 517–520.
56 W. Gong and A. Navrotsky, Thermodynamics of $BaNd_2O_4$ and phase diagram of the $BaO–Nd_2O_3$ system, *J. Mater. Res.*, 2019, **34**(19), 3337–3342.
57 D. L. Drey, E. C. O'Quinn, T. Subramani, K. Lilova, G. Baldinozzi, I. M. Gussev, A. F. Fuentes, J. C. Neufeind, M. Everett, D. Sprouster, A. Navrotsky, R. C Ewing and M. Lang, Disorder in $Ho_2Ti_{2-x}Zr_xO_7$: pyrochlore to defect fluorite solid solution series, *RSC Adv.*, 2020, **10**(57), 34632–34650.
58 S. Hayun and A. Navrotsky, Formation enthalpies and heat capacities of rear earth titanates: RE_2TiO_5 (RE = La, Nd and Gd), *J. Solid State Chem.*, 2012, **187**, 70–74.
59 M. Abramchuk, K. Lilova, T. Subramani, R. Yoo and A. Navrotsky, Development of high-temperature oxide melt solution calorimetry for p-block element containing materials, *J. Mater. Res.*, 2020, **35**(16), 2239–2246.
60 T. Subramani, K. I. Lilova, M. Householder, S. Yang, J. Lyons and A. Navrostky, Surface energetics of wurtzite and sphalerite polymorphs of zinc sulfide and implications for their formation in nature, *Geochim. Cosmochim. Acta*, 2023, **340**, 99–107.
61 A. Mielewczyk-Gryn and A. Navrotsky, Enthalpies of formation of rare earth niobates, RE_3NbO_7, *Am. Mineral.*, 2015, **100**(7), 1578–1583.
62 S. Hayun, K. Lilova, S. Salhov and A. Navrotsky, Enthalpies of formation of high entropy and multicomponent alloys using oxide melt solution calorimetry, *Intermetallics*, 2020, **125**, 106897.
63 A. Navrotsky, W. Lee, A. Mielewczyk-Gryn, S. V. Ushakov, A. Anderko, H. Wu and R. E. Riman, Thermodynamics of solid phases containing rare earth oxides, *J. Chem. Thermodyn.*, 2015, **88**, 126–141.
64 R. A. Robie and B. S. Hemingway, *Thermodynamic properties of minerals and related substances at 298.15 K and 1 bar (105 Pascals) pressure and at higher temperatures*, US Government Printing Office, 1995, vol. 2131.
65 A. Mielewczyk-Gryń, T. Subramani, D. Jaworski, K. Lilova, W. Skubida, A. Navrotsky and M. Gazda, Water uptake and energetics of the formation of barium zirconate based multicomponent oxides, *Phys. Chem. Chem. Phys.*, 2023, **25**(13), 9208–9215.

